A Systematic Study of How Different Phases of Niobium Nitride (Nb_xN) React to Xenon Difluoride (XeF_2) Undercut Etch

2023 CNF REU Intern: Daniel Joel Harrison
Intern Affiliation: Electrical and Computer Engineering, Morgan State University

2023 CNF REU Principal Investigator: Professor Debdeep Jena, Electrical and Computer Engineering, Cornell

2023 CNF REU Mentor: Wenwen Zhao, Applied and Engineering Physics, Cornell University

Program & Primary Source of Research Funding: 2023 Cornell NanoScale Facility Research Experiences for Undergraduates (CNF REU) Program via the National Science Foundation under Grant No. NNCI-2025233

Contact: dahar73@morgan.edu, djena@cornell.edu, wz344@cornell.edu

Website(s): https://cnf.cornell.edu/education/reu/2023

Primary CNF Tools Used: ABM Contact Aligner, Glen 1000 Resist Strip, SC4500 Electron Beam Evaporator, Xactix Xenon Difluoride Etcher, Bruker Energy-dispersive X-ray Spectrometer (EDS), Zygo 3D Optical Profilometer

Abstract:

The superconducting niobium nitride (NbN) was successfully integrated epitaxially with the III-nitride heterostructures (AlN, GaN, etc.) recently [1]. This new technology opens the possibilities for epitaxial metal/semiconductor Schottky diodes, epitaxial gate junctions for III-nitride transistors as well as all-epitaxial bulk acoustic wave resonators. The metallic epitaxial NbN also offers a way to be selectively etched chemically, which allows the lift-off of the epilayers or devices.

The NbN system is complex and presents various phases (i.e., beta, delta, epsilon, and gamma) [2]. Here in this work, by taking advantage of the high crystalline quality niobium nitride (Nb_xN) films grown by molecular-beam epitaxy (MBE), we propose to do a conclusive study to understand the xenon difluoride (XeF_2) undercut etch characteristics of different phases of Nb_xN. This study identifies the prerequisite conditions for the epilayer lift-off with a sacrificial layer of Nb_xN.

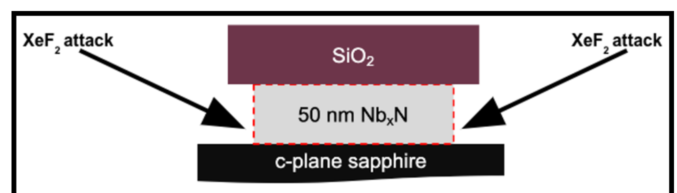

Figure 1: Cross-sectional representation of undercut process.

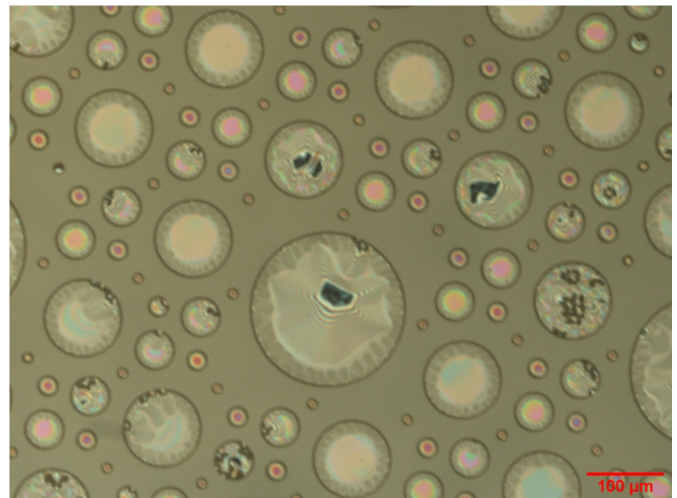

Figure 2: Delta phase niobium nitride after full undercutting at 4 Torr XeF_2 pressure.

Summary of Research:

The Nb_xN films were epitaxially grown on 2-inch sapphire wafers. The Nb_xN phases used in this study are Delta phase grown at 600°C, Epsilon phase grown at 700°C, Gamma phase grown at 800°C, and Beta phase grown at 1000°C.

The Nb_xN samples were cut into 1 cm × 1 cm pieces. A total number of 12 samples were used for this research. Photolithography was done to develop a pattern of different sized circular pads ranging from 12.5 μm to 200 μm in diameter. To have a better visualization of the etch process, a transparent silicon dioxide (SiO_2) mask was deposited on the samples using an electron beam evaporator.

A XeF_2 etcher was used for the undercut etch process. Reference [3] indicates that the XeF_2 undercut etch rate increases with the increase of chamber temperature. The chamber temperature in this work was accordingly set at 100°C, which is the highest temperature the current etcher can achieve. Each sample for each phase was etched at a different XeF_2 pressure (4 Torr, 3 Torr and 2 Torr) for understanding the impact of the XeF_2 partial gas pressure on the undercut etch rate. It was observed that the vertical etching of Nb_xN by XeF_2 was done effortlessly, i.e., the Nb_xN not covered by SiO_2 would be etched away after the first etch cycle. The difficulty then was for the XeF_2 to go under the SiO_2 membranes

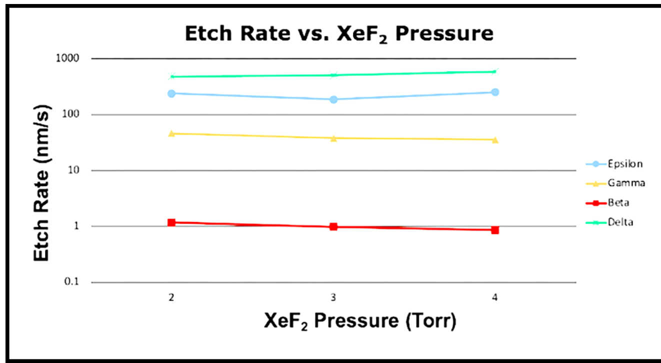

Figure 3: Average etch rates as a function of XeF_2 pressure for all four phases of Nb_xN.

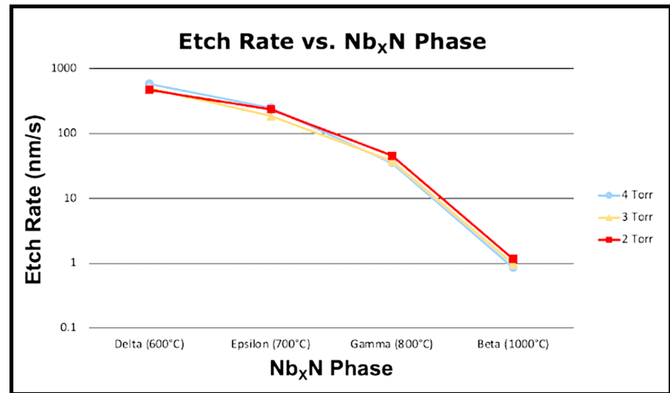

Figure 4: Average etch rates as a function of Nb_xN phase.

as seen in Figure 1 to attack the Nb_xN. This undercut etch will result in the release of the SiO_2 membranes. All the samples in this study experienced vertical etching of Nb_xN, but not all experienced a complete undercut of Nb_xN.

The samples of Delta phase were fully undercut after 70 seconds as seen in Figure 2. A change in the average etch rate was observed, which was proportional to the change of the XeF_2 pressure. Similarly, the samples of Epsilon phase were fully undercut after 3-4 minutes. There was no direct correlation of etch rates and XeF_2 pressure observed for Epsilon phase, but it was noticed that the average etch rates increased overtime.

The undercut etch of Gamma phase Nb_4N_3 at 4 Torr and 3 Torr XeF_2 pressure were not completely released after 12 minutes. Differently, a duality was seen at 2 Torr XeF_2 pressure, in which case some membranes became close to being fully undercut after 12 minutes. Unfortunately, most membranes became darker over time, implying that the reaction between XeF_2 and Gamma phase Nb_xN is unstable and unpredictable. The initial average etch rates for Gamma phase Nb_4N_3 decreased as the XeF_2 pressure increase, but overtime the etch rates went to zero, as none of the samples were fully undercut.

No full undercut for any of the samples for Beta phase Nb_2N was seen even after 14 minutes. Similar to Gamma phase, the initial average etch rates for Beta phase Nb_2N decreased as the XeF_2 pressure increased, but overtime the etch rates went to zero, as none of the samples were fully undercut.

Figure 3 shows how the average etch rate for each phase changes as the XeF_2 pressure increases. Figure 4 shows how the average etch rates changes as we move through the different Nb_xN phases. It was noticed that Nb_xN films grown at higher MBE temperatures are more difficult to be fully undercut by XeF_2.

Conclusions and Future Steps:

Results from the research show that Delta and Epsilon phase Nb_xN can be fully undercut by XeF_2; Gamma phase Nb_xN does exhibit some XeF_2 undercut capabilities, but the reaction is unstable and unpredictable; Beta phase Nb_xN cannot be fully undercut by XeF_2. In general, Nb_xN phases grown at higher MBE temperatures are more difficult to be fully undercut by XeF_2.

This research is a preliminary step to help us understand the required conditions for doing an epitaxial lift-off of high-quality aluminum nitride (AlN) membranes. The next step is a research project titled: "Monolithic integration of acoustic resonators and high electron mobility transistors (HEMTs) utilizing aluminum nitride platform." For this project, we will fabricate acoustic resonators from AlN using Delta or Epsilon phase Nb_xN as a sacrificial layer.

Acknowledgements:

This work was performed in part at the Cornell NanoScale Facility, an NNCI member supported by NSF Grant NNCI-2025233. Special thanks to Professor Debdeep Jena, Professor Huili (Grace) Xing, Wenwen Zhao, Melanie-Claire Mallison, Aaron Windsor, and Professor Michael Spencer. This work would not have been successful without their guidance.

References:

[1] Yan, R., Khalsa, G., Vishwanath, S. et al. GaN/NbN epitaxial semiconductor/superconductor heterostructures. Nature 555, 183-189 (2018). https://doi.org/10.1038/nature25768.

[2] Wright, J., Xing, H., Jena, D. Growth windows of epitaxial Nb_xN films on c-plane sapphire and their structural and superconducting properties. (2022) https://arxiv.org/pdf/2203.14083.pdf.

[3] Brian P. Downey, et al., XeF_2 etching of epitaxial Nb_2N for lift-off or micromachining of III-N materials and devices. Journal of VS&T A 1 September 2017; 35 (5): 05C312. https://doi.org/10.1116/1.4994400.

Design and Implementation of an AlScN-Based FeMEMS Multiplier for In-Memory Computing Applications

CNF Project Number: 1121-03
Principal Investigator(s): Amit Lal
User(s): Shubham Jadhav

Affiliation(s): School of Electrical and Computer Engineering, Cornell University

Primary Source(s) of Research Funding: Defense Advanced Research Projects Agency (DARPA), Tunable Ferroelectric Nitrides (TUFEN)

Contact: amit.lal@cornell.edu, saj96@cornell.edu

Website(s): http://www.sonicmems.ece.cornell.edu/

Primary Tools Used: SUS MA-6 contact aligner, CVC SC-4500 Odd-hour evaporator, Zeiss SEM, OEM Endeavor M1, Plasma-Therm Takachi HDP-CVD, Arradiance ALD, AJA sputter deposition, Oxford PECVD, Oxford 81/82, Primaxx Vapour HF Etcher, PT770 Etcher, YES EcoClean Asher, Xactix Xenon Difluoride Etcher, AJA ionmill, Heidelberg Mask Writer-DWL2000, P7 Profilometer, Zygo Optical Profilometer, Flexus Film Stress Measurement

Abstract:

This paper reports on the design, fabrication, and experimental validation of an aluminum scandium nitride (AlScN) based Ferroelectric Micro-Electro-Mechanical Systems (FeMEMS) Multiplier — a core component for multiply-accumulate (MAC) operations in next-generation in-memory computing applications. The FeMEMS multiplier leverages ferroelectric polarization switching in AlScN to change the piezoelectric coefficient (d_{31}), facilitating non-volatile, analog memory storage for weights in a neural network. The piezoelectric parameters of the films are then used to change a capacitive gap for readout. The ferroelectric thin films could be partially polarized and reached a peak remnant polarization of 216 μC/cm^2 at a voltage of 100V V_P (5MV/cm). Experimental results on optically measured displacements confirmed the AlScN unimorph multiplier's operation. The maximum resonance mode displacement was linearly dependent on the polarization and input voltages. This work provides foundational insights into the utilization of AlScN in in-memory computing, opening new avenues for high-speed, low-power, and high-accuracy computing applications.

Summary of Research:

To address the computational limitations of traditional von-Neumann architectures, researchers are exploring in-memory computing. A fundamental building block of this approach is the MAC unit, which is capable of performing matrix multiplication and summative operations [1]. The research highlights the potential of micro and nanoelectromechanical systems (M/NEMS) to provide zero standby leakage power and offer efficient computation [2,3].

The recently discovered ferroelectricity in scandium-alloyed aluminum nitride (AlScN) has enabled the implementation of MEMS MAC units in III-V systems [4,5]. This research presents the design, fabrication, and characterization of a ferroelectric aluminum scandium nitride (AlScN) based programmable nano-electromechanical system (NEMS) multiply and accumulate (MAC) unit.

A 500 μm Si substrate wafer was used to fabricate the ferroelectric unimorph. A 1 μm thermal SiO_2 layer serves as the elastic layer. Next, a continuous layer of sputtered 200 nm Pt was deposited as the bottom electrode. A ferroelectric AlScN film, with a thickness of 200 nm and 22% Sc content, was deposited on this Pt electrode. This film stack was achieved through reactive co-sputtering of scandium (Sc) and aluminum (Al) in a nitrogen environment. Next, a lift.off process was employed to evaporate 10nm/100nm Cr/Au metal top electrodes. Reactive ion-etching and ion-milling were then used to etch through the thin-film stack to fabricate etch-holes for releasing the unimorph. This step was followed by a vapor-phase bulk isotropic etching of the underlying silicon substrate using XeF_2 to release the unimorph. This process flow resulted in the successful creation of released cantilevers, clamped-clamped beams, and membranes, all on the same wafer (Figure 1).

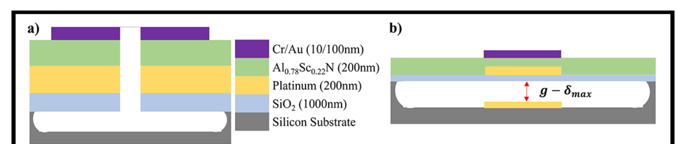

Figure 1: Schematic cross-section view of the FeNEMS.

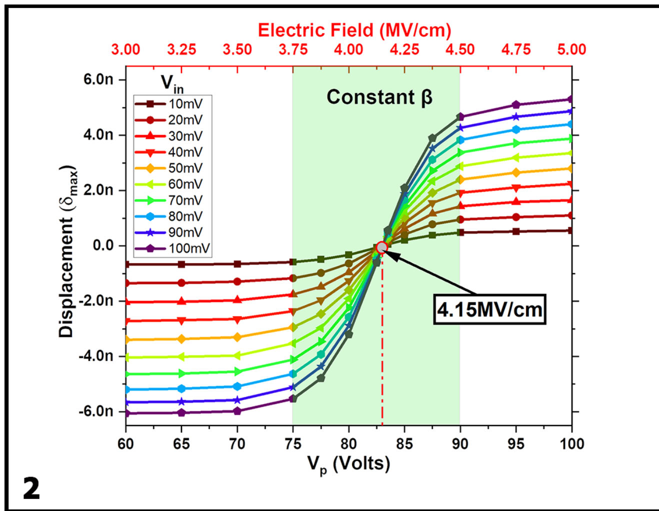

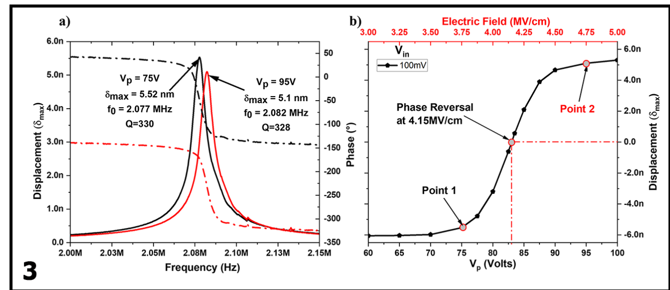

Figure 2, left: The transfer characteristics of the FeMEMS multiplier device. Figure 3, above: Magnitude and phase plot of state 1 (depicted in black) and state 2 (in red) versus frequency, illustrating the characteristic ferroelectric domain reversal phenomenon.

The device operation is based on the principle of partial polarization switching in AlScN. The polarization-switching voltage (V_P) is used to define the weights of the MAC operation. The piezoelectric coefficient (d_{31}) can be tuned by applying varying V_P voltages. The polarization switching was studied using a Radiant Technologies Precision Premier II Ferroelectric Tester. An increase in VP resulted in a gradual increase in the remnant polarization (P_r) until a maximum of $2P_r$ = 216 μC/cm^2 at V_P = 100V (5 MV/cm).

Once the weights are programmed by applying V_P voltages, the input voltage (V_{in}) is fed to the device to generate an output. The device behaves as a multiplier, where the maximum out-of-plane displacement (δ_{max}) of the unimorph actuator is a scaled product of the V_P and V_{in}. This displacement was measured using a Polytec MSA-400 Laser Doppler Vibrometer (LDV). The device functionality was verified by measuring δ_{max} as a function of V_P and V_{in}. The measurements showed a linear relationship between δ_{max} and the product of V_P and V_{in} for V_P and V_{in} in the range of 75V to 90V, confirming the multiplication operation (Figure 2).

For V_P values greater than the threshold, the polarity of δ_{max} changed, which indicates a reversal in the polarization of the AlScN. This causes a phase change in the unimorph response. This was verified by recording a phase reversal around the V_P = 83.5V, resulting in a zero displacement at this point with a complete phase inversion on either side (Figure 3).

Conclusions:

This research presents an innovative design of a Ferroelectric AlScN-based NEMS MAC unit, leveraging partial polarization switching in AlScN for in-memory computing. This approach enhances latency, power consumption, and operational efficiency in wideband gap III-V platforms, demonstrating the unit's ability to effectively store multi-level computational weights. The device's function as a multiplier was validated through a correlation between maximum displacement, polarization, and applied voltages. Notably, phase reversal was observed at V_P = 83.5V (4.15MV/cm), indicating the device's versatility. The FeMEMS multiplier's minimal standby leakage power and compatibility with III-V platforms enhance its overall efficiency. This study paves the way for future exploration of AlScN in high-speed, low-power, and high-accuracy computing applications, as well as advancements in zero standby power computing.

References:

[1] C. Mead, "Neuromorphic Electronic Systems," Proc. IEEE, vol. 78, no. 10, pp. 1629-1636, 1990.

[2] S. Jadhav, V. Gund, B. Davaji, D. Jena, H. (grace) Xing, and A. Lal, "HZO-based FerroNEMS MAC for in-memory computing," Appl. Phys. Lett., vol. 121, no. 19, p. 193503, Nov. 2022.

[3] S. Jadhav, V. Gund, and A. Lal, "Programmable Ferroelectric HZO NEMS Mechanical Multiplier for in-Memory Computing," 2023 IEEE 36th Int. Conf. Micro Electro Mech. Syst., pp. 519-521, Jan. 2023.

[4] S. Fichtner, N. Wolff, F. Lofink, L. Kienle, and B. Wagner, "AlScN: A III-V semiconductor based ferroelectric," J. Appl. Phys., vol. 125, no. 11, p. 114103, Mar. 2019, [Online]. Available: http://aip.scitation.org/doi/10.1063/1.5084945.

[5] D. Jena, et al., "The new nitrides: layered, ferroelectric, magnetic, metallic and superconducting nitrides to boost the GaN photonics and electronics eco-system," Jpn. J. Appl. Phys., vol. 58, no. SC, p. SC0801, May 2019.

Fabrication and Manipulation of Micro-Scale Opto-Electrically Transduced Electrodes (MOTEs) for Electrochemical and Neural Activity Measurements

CNF Project Number: 2658-18, 2836-19
Principal Investigator(s): Prof. Alyosha C. Molnar
User(s): Shahaboddin Ghajari, Sanaz Sadeghi, Devesh Khilwani

Affiliation(s): Electrical and Computer Engineering, Cornell University
Primary Source(s) of Research Funding: National Institute of Health
Contact: am699@cornell.edu, sg2367@cornell.edu, ss3842@cornell.edu, dk842@cornell.edu
Website(s): https://molnargroup.ece.cornell.edu/
Primary CNF Tools Used: ABM Contact Aligner, AJA Sputter, Westbond 7400A Ultrasonic Wire Bonder, Oxford 100, Oxford 81, Oxford 82, Unaxis Deep Si Etcher, Oxford PECVD, Oxford ALD, Anatech, P7 Profilometer, ZEISS Ultra and Supra SEMs

Abstract:

Microscale wireless sensors are beneficial in many applications such as electrochemical measurements and neural recordings. Recording neural activity in live animals *in vivo* is critical in elucidating how the brain functions. However, such recording poses several challenges. Electrical techniques typically require electrodes to be tethered to the outside world directly via a wire, or indirectly via an RF Coil [1], which is much larger than the electrodes themselves. Tethered implants suffer from the residual motions between electrodes and neurons as the brain moves, limiting our ability to measure peripheral nerves in moving animals. On the other hand, optical techniques, which are becoming increasingly potent [2], are often limited to subsets of neurons in any given organism, impeded by scattering of the excitation light and emitted fluorescence, and limited to low temporal resolution [3]. Here we present an untethered opto-electrical system on chip (SoC), Micro-scale Opto-electrically Transduced Electrodes (MOTEs), which are powered by, and communicating through a microscale optical interface, combining many benefits of optical techniques with high temporal-resolution of electrical recording. We also introduce an electrochemical platform similar to MOTE which is called Redox Enabled Micro-scale Opto-electrically Transduced Electrodes (ReMOTEs), which we used for pH measurements.

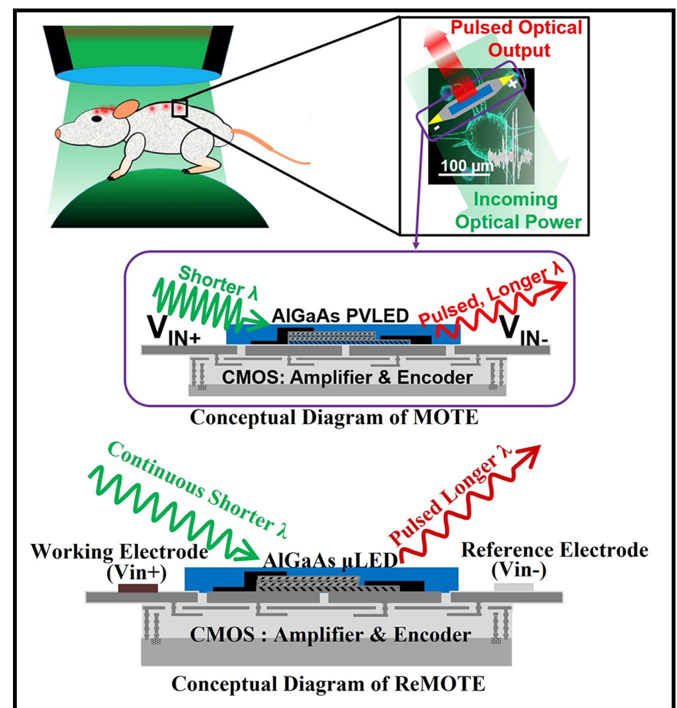

Figure 1: An exemplary implementation and system level description of the MOTEs and ReMTOEs [4,5].

Summary of Research:

Our fabrication starts with a conventional 180 nm CMOS die, which contains the electronics for signal amplification, encoding, and transmission. The CMOS die is then integrated with AlGaAs diode, which acts as a photo-voltaic (PV) as well as light emitting diode (LED), hence the diode is abbreviated as PVLED. The PVLED provides an optical link which powers the electronics and transmits encoded signals in optical pulses. The MOTE utilizes Pulse Position Modulation (PPM) for signal encoding for its high information-per-photon efficiency, where the spacing between the output pulses is proportional to the measured electric field of neuronal or electrochemical signals across the measurement electrodes. Figure 1 depicts a conceptual deployment and system description of such MOTE [4,5]. It should be noted that preliminary electrochemical pH measurement results for ReMOTE are presented in [5]; however, the release process is not performed on it.

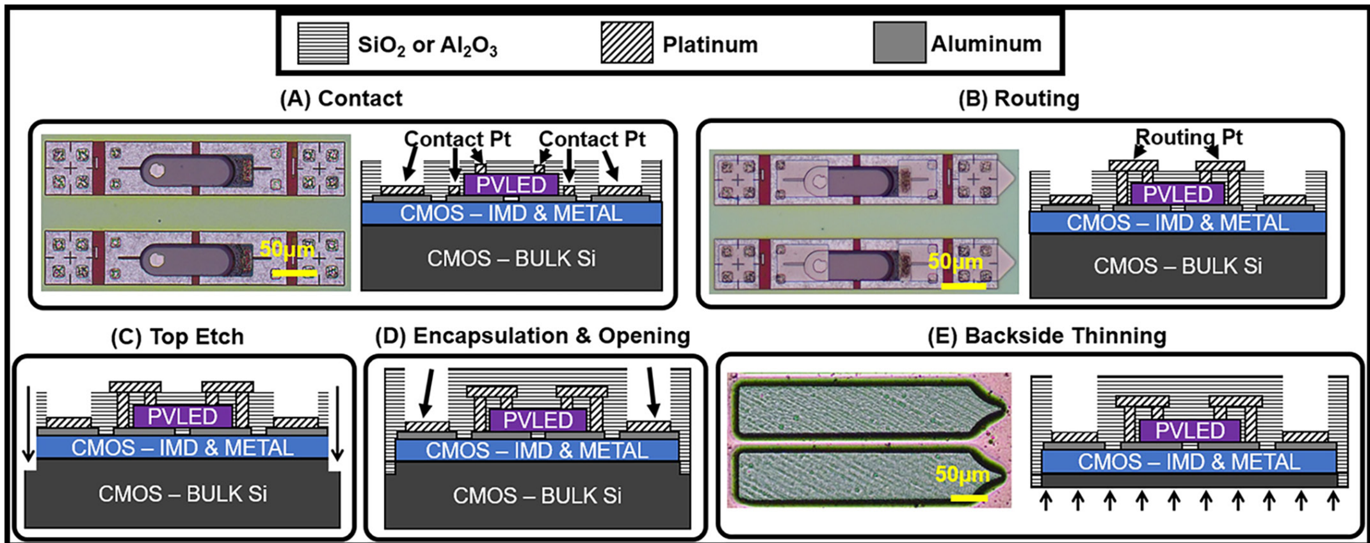

Figure 2: MOTE Fabrication Process. (A) An AlGaAs µLED (bullet-shaped) array is transferred on top of a CMOS chip containing an array of unit MOTE circuitry, and Pt is deposited over contact areas. (B) Routing Pt electrically connects each µLED with an underlying CMOS. (C) Each MOTE is segregated and (D) encapsulated with SiO_2 and Al_2O_3 except for the measurement electrodes area. (E) The backside Si is thinned so that total thickness is < 30 µm. Adapted from [6].

The AlGaAs diodes are first fabricated on a sapphire wafer, to be later released from the sapphire substrate with a sacrificial Poly (methyl methacrylate) (PMMA) polymer. Once the PMMA-coated AlGaAs diodes are transferred onto the CMOS die, Oxford 81 plasma etcher is used to remove the sacrificial PMMA, leaving only the diodes array intact on the CMOS die. To establish the electrical contact between the PVLED and CMOS, we have used CNF ABM Contact Aligner for photolithography with AZ nLof2020 UV photoresist for efficient lift-off process that ensues after metal deposition. After the contact fabrication, the contacts of CMOS and PVLED are connected via similar photo-lithography process, and to maximize the conformality of the metal routing, we employ AJA Sputter. Following the routing step, each MOTE is encapsulated using OXFORD ALD and PECVD for SiO_2 and Si_3N_4 deposition, followed by dielectric etching using OXFORD 100 and UNAXIS Deep Reactive Ion Etch (DRIE) for release. Figure 2 describes the fabrication sequence described herein.

It should be noted that before embarking on the nano/micro-fabrication flow, to confirm the functionality of each module (CMOS and the diode), we use the Westbond 7400A Ultrasonic Wire Bonder for board-level test. ZEISS Ultra and Supra Scanning Electron Microscopes (SEMs) are also used to inspect the fabricated MOTE for debugging purposes.

Conclusions and Future Steps:

MOTEs are the smallest electrophysiological sensor of its kind, and we are currently testing the MOTEs *in vivo* in mouse animal models. As we accumulate more data on our ongoing *in vivo* efforts, we plan to improve fabrication processes as well as surgical procedures for inserting the MOTEs into the mouse cortex. We also presented preliminary results for electrochemical measurements, and we plan to combine the sensors with micro-robots.

References:

[1] Harrison RR, Watkins PT, Kier RJ, Lovejoy RO, Black DJ, Greger B, and Solzbacher F. A Low-Power Integrated Circuit for a Wireless 100-Electrode Neural Recording System. IEEE J. Solid-State Circuits. 2006 Dec 26;42(1): 123-133.

[2] A. C. Molnar, S. Lee, A. Cortese, P. McEuen, S. Sadeghi and S. Ghajari, "Nanoliter-Scale Autonomous Electronics: Advances, Challenges, and Opportunities," 2021 IEEE Custom Integrated Circuits Conference (CICC), Austin, TX, USA, 2021, pp. 1-6, doi: 10.1109/CICC51472.2021.9431529.

[3] Yang W and Yuste R. *In vivo* Imaging of Neural Activity. Nature Methods. 2017 Mar 31;14(4):349-359.

[4] Lee S, Cortese AJ, Trexel P, Agger ER, McEuen PL, and Molnar AC. A 330 µm × 90 µm Opto-Electronically Integrated Wireless System-on-chip for Recording of Neural Activities. IEEE ISSCC. 2018 Feb.

[5] S. Ghajari, S. Lee, S. Norris, P. McEuen, A. Molnar, "Redox-Enabled Microscale Opto-Electronically Transduced Electrodes (ReMOTEs)", 2023 IEEE International Symposium on Circuits and Systems (ISCAS), Monterey, CA, USA, 2023.

[6] Lee S, Cortese AJ, Mok A, Wu C, Wang T, Park JU, Smart C, Ghajari S, Khilwani D, Sadeghi S, Ji Y, Goldberg JH, Xu C, McEuen PL, and Molnar AC. Fabrication of Injectable Micro-Scale Optoelectronically Transduced Electrodes (MOTEs) for Physiological Monitoring. IEEE JMEMS. 2020 June 12;29(5):720-726.

Cross-Plane Thermal Conductivity of *h*-BN Thin Films Grown by Pulsed Laser Deposition

CNF Project Number: 2758-19
Principal Investigator(s): Zhiting Tian
User(s): Gustavo A. Alvarez, Jinha Kwon

Affiliation(s): Sibley School of Mechanical and Aerospace Engineering, Cornell University

Primary Source(s): Department of the Navy, Office of Naval Research

Contact: zt223@cornell.edu, gaa78@cornell.edu
Website(s): https://ztgroup.org/

Primary CNF Tools Used: SC4500 Odd-Hour Evaporator, P7 Profilometer, AFM-Veeco Icon

Abstract:

The distinguished properties of *h*-BN, specifically its atomically smooth surface, large critical electric field, and large electronic band gap, make it ideal for thin film microelectronics and as an ultrawide bandgap (UWBG) semiconductor. Owing to weak van der Waals interactions between layers, *h*-BN exhibits a significant degree of anisotropic thermal conductivity (κ). Exfoliation from bulk crystals is not a sustainable method for mass production of *h*-BN due to its low repeatability, low yield, poor control of sample thickness, and limitation to small areas. Thus, it is necessary to investigate the thickness-dependence of $\kappa_{\perp}$ for thin films grown by a practical growth method, such as pulsed laser deposition (PLD), which enables the production of reliable and large-area *h*-BN films with control of film thickness. We grew *h*-BN using PLD at 750°C and observed a non-monotonic trend of $\kappa_{\perp}$ as thickness increased from 30 nm to 300 nm, varying from ~ 1.47 to ~ 0.19 W/(mK). We observed a high $\kappa_{\perp}$ value for *h*-BN at a thickness of 30 nm, providing insights into the $\kappa_{\perp}$ of PLD-grown films suitable for electronics applications.

Summary of Research:

The continued scaling down of device dimensions [1] and operation in high-voltage or high-frequency regimes aggravates thermal loads, and effective heat dissipation has become one of the most critical challenges in device performance and reliability [2]. Hexagonal boron nitride (*h*-BN) is a two-dimensional (2D) material with excellent properties for the thermal management of next-generation electronics. Existing literature regarding the thermal conductivity (κ) of *h*-BN films typically focuses on the in-plane thermal conductivity ($\kappa_{\parallel}$) and samples produced by the exfoliation from bulk *h*-BN. The $\kappa_{\parallel}$ of few-layer *h*-BN nanosheets falls in the range of 100 -360 W/(mK) at room temperature [3].

Owing to weak van der Waals interactions between layers, *h*-BN has a highly anisotropic κ. The only measured data of the cross-plane thermal conductivity ($\kappa_{\perp}$) of *h*-BN is 0.2 to 8.1 W/(mK) between 7 nm to 585 nm, respectively, for *h*-BN flakes exfoliated at room temperature [4]. Exfoliation from bulk crystals is not a sustainable method for mass production, thus there is a need to investigate the thickness-dependent $\kappa_{\perp}$ for a scalable growth method, which provides reliable and large-area *h*-BN with control of film thickness.

We utilized pulsed laser deposition (PLD), which offers several benefits compared to other growth methodologies. PLD involves the deposition of thin films from a single polycrystalline target directed upon the substrate, therefore ensuring the preservation of stoichiometry throughout the deposition process. We measured $\kappa_{\perp}$ of *h*-BN thin films ranging from 30 nm to 300 nm implementing the optical pump-probe method, frequency-domain thermoreflectance (FDTR), depicted in Figure 1a. The samples were modeled as a three-layer system, with each layer defined by the layer thickness, volumetric heat capacity c_p, the thermal boundary conductances G1 and G2, the $\kappa_{\perp}$ and in-plane thermal conductivity ($\kappa_{\parallel}$). To maximize the coefficient of thermoreflectance of the 532 nm probe, Au was chosen as the transducer layer and the SC4500 Odd-Hour Evaporator at CNF was utilized to deposit a 100 nm layer of Au (thickness determined by the P7 profilometer).

Two curves are plotted in Figure 2a, assuming lower and higher bounds of $\kappa_{\parallel}$. Despite the slight increase of $\kappa_{\perp}$ for the isotropic case and for film thicknesses ≤ 50 nm, the $\kappa_{\perp}$ of the *h*-BN thin films decrease from 1.47 to 0.19 W/(mK) with an increase in film thickness from 30 nm to 300 nm. Previous experiments observed long phonon mean free path > 100 nm for $\kappa_{\perp}$ of exfoliated *h*-BN flakes; predictions by first-principles calculations indicated ~ 80% of the heat is transported by phonons of MFPs ranging from 3 nm to 90 nm [4].

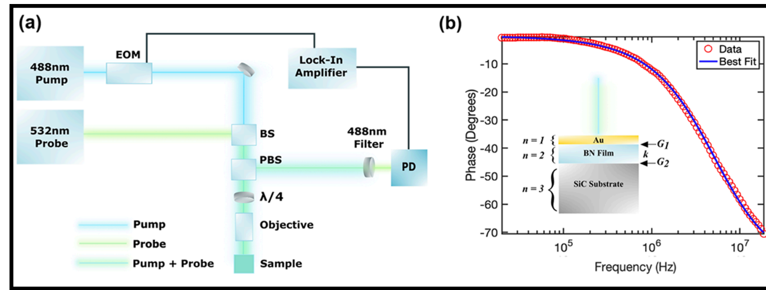

Figure 1: FDTR experimental setup and fitted data. (a) Simplified schematic of the FDTR system. (b) Phase vs. frequency data obtained from FDTR measurements for the 50 nm epitaxial h-*BN layer on bulk SiC substrate.*

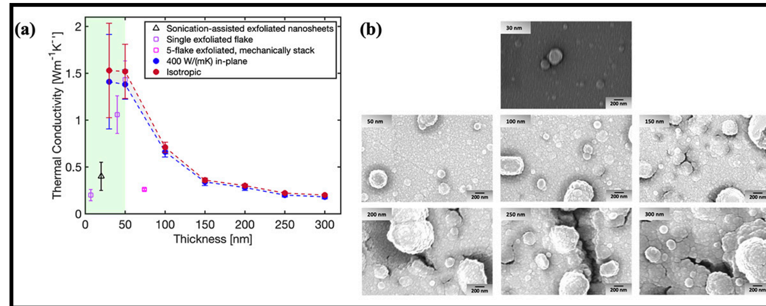

Figure 2: Thickness-dependent thermal conductivity and SEM of h-*BN films. (a) As the thickness of the thin film increases there is a decrease in sample quality, thus, reducing* $\kappa_\perp$ *(b) Crack propagation is evident as the thickness increases leading to an increase in phonon defect scattering.*

If the film quality of PLD-grown h-BN was consistent across the thickness range, we should expect the $\kappa_\perp$ increases, at least up to 100 nm, with thickness due to the size effect. However, our findings indicate the opposite trend, implying that as the thickness of the film increases, there is a significant decrease in the film quality.

To investigate the quality of the thin films, a commercial AFM system was utilized. An increase in root-mean-square (RMS) from 3.30 nm to 17.40 nm for the *h*-BN films with a thickness from 30 nm to 300 nm was determined. The increase in RMS presents increasing surface roughness, which introduces stronger phonon scattering, thereby reducing $\kappa_\perp$.

Lastly, the Zeiss Gemini 500 Scanning Electron Microscope (SEM) was utilized to capture high-resolution images of the sample surfaces, as shown in Figure 2b. As thickness increases, voids/cracks start to form and are evident in the thicker *h*-BN films, which leads to strong phonon-defect scattering, thereby reducing $\kappa_\perp$.

In conclusion, among two-dimensional materials (2D), hexagonal boron nitride (*h*-BN) stands out as a highly promising candidate for use in both micro and nanoscale devices, given its exceptional mechanical, electrical, and thermal properties. The PLD-grown *h*-BN at 30 nm showed a larger $\kappa_\perp$ value than that of the single exfoliated flake at 7 nm and 40 nm [4], and a larger value that of the sonicated-assisted exfoliated nanosheets at 20 nm [5]. These thinner samples provide the high $\kappa_\perp$, suitable for integrated circuits and high-power electrics, which are in need of heat dissipation while maintaining a compact and lightweight design.

References:

[1] Ferain, I., Colinge, C., and Colinge, J. Nature, 310-316 (2011).
[2] Balandin, A. IEEE Spectr 46, 34-39 (2009).
[3] Jiang, P., Qian, X., and Yang, R. RSI 88, 074901 (2017).
[4] Jaffe, G. R., et al. Condensed Matter (2021).
[5] Wang, Y., et al. Nanoscale 10, 167-173 (2017).

First Demonstration of AlBN/GaN High Electron Mobility Transistors

CNF Project Number: 2800-19
Principal Investigator(s): Huili Grace Xing, Debdeep Jena
User(s): Kazuki Nomoto

Affiliation(s): School of Electrical & Computer Engineering, Cornell University

Primary Source(s) of Research Funding: ARO

Contact: grace.xing@cornell.edu, kn383@cornell.edu

Primary CNF Tools Used: Autostep i-line Stepper (GCA AS200), Heidelberg Mask Writer DWL2000, P7 Profilometer, FilMetrics, AFM Veeco Icon, Zeiss SEM, PT770, Oxford81, Oxford PECVD, Oxford ALD, SC4500 Evaporators, AJA Sputter Deposition tools, RTA AG610, JEOL 9500

Abstract:

Epitaxial aluminum boron nitride (AlBN) is a potential barrier material for gallium nitride (GaN) high electron mobility transistors (HEMTs) due to large energy bandgap high-κ dielectric properties [1,2]. This work reports the first demonstration of AlBN/GaN HEMTs.

Summary of Research:

A 2 nm GaN passivation layer / 2 nm AlBN high-κ barrier / 600 nm GaN channel / 125 nm AlN buffer structure was grown on a 6H silicon carbide substrate using plasma-assisted molecular beam epitaxy (PA-MBE) (Figure 1(a)). Hall-effect measurements at room temperature revealed a two-dimensional gas (2DEG) sheet concentration of 9.25×10^{12} /cm^2, electron mobility of 524 cm^2/V·s, and sheet resistance of 1290 Ω/sq.

First, BCl_3 inductively coupled plasma (ICP) etching was performed for device isolation, followed by ohmic metallization. A Ta/Al/Ni/Au (20/150/50/50 nm) metal stack was deposited using an electron-beam evaporator (SC4500) and alloyed in N_2 ambient using a rapid thermal annealing system (RTA AG610). The resulting contact resistance was ~ 2 Ω·mm. A gate metal stack of Ni/Au (30/220 nm) was deposited directly on the sample surface using SC4500. Gate lengths were defined via photolithography (L_g = 1.3 μm) using an Autostep i-line stepper (GCA AS200).

Figure 1(b) shows the scanning electron microscope (SEM) image of the completed AlBN/GaN HEMT.

Figure 2 shows the 500 kHz *C-V* results of AlBN/GaN and AlN/GaN Schottky barrier diodes. The extracted dielectric constants of AlBN from on-wafer capacitance measurements at various frequencies exibit higher values than AlN.

Figure 3(a) shows the measured output characteristics of the AlBN/GaN HEMTs of 1.3 μm gate length, and 2.3 μm source-drain distance. The saturated on-current reaches 266 mA/mm, and repeatable current saturation, pinch-off, and similar performance is measured for several devices of similar size. Figure 3(b) shows the transfer characteristics of the Schottky-gated AlBN/GaN HEMTs, which exhibit an on/off ratio of > 10^3. Since this is limited by the gate leakage of the Schottky diode. Figure 3(b) also shows the threshold voltage of -0.5 V and the subthreshold slope of 150 mV/dec. Figure 3(c) shows a peak $gm_{,ext}$ of 139 mS/mm, all at room temperature. The promising first AlBN/GaN HEMT performance will be boosted by higher mobility in the future.

References:

[1] Chandrashekhar Savant, et al., 65th EMC, O10 (2023).
[2] J. Hayden, et al., Physical Review Materials, 5, 044412 (2021).

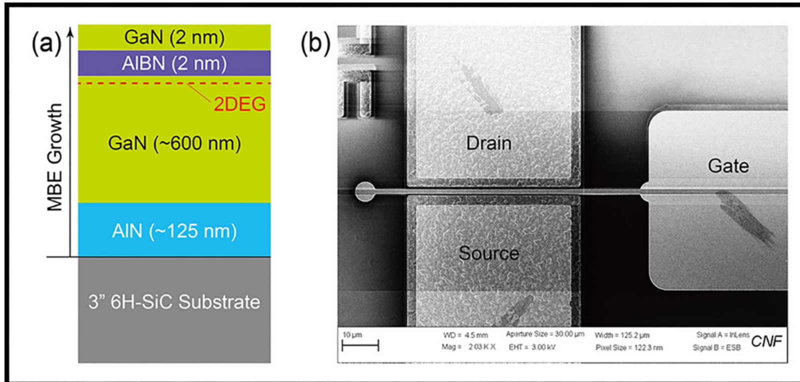

Figure 1: (a) Layer structure of the epitaxial film grown by MBE, dashed line indicating where a high-density 2D electron gas (2DEG) is present. (b) 70° angled-view SEM image of the fabricated AlBN/GaN HEMT with L_g *= 1.3 µm,* W_g *= 50 µm, and* L_{sd} *= 2.3 µm.*

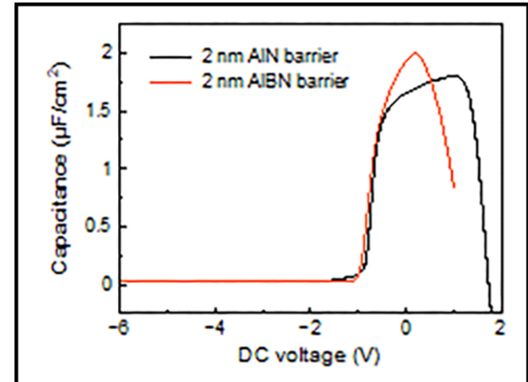

Figure 2: C-V *data at 500 kHz of AlBN and AlN showing higher dielectric constant of AlBN.*

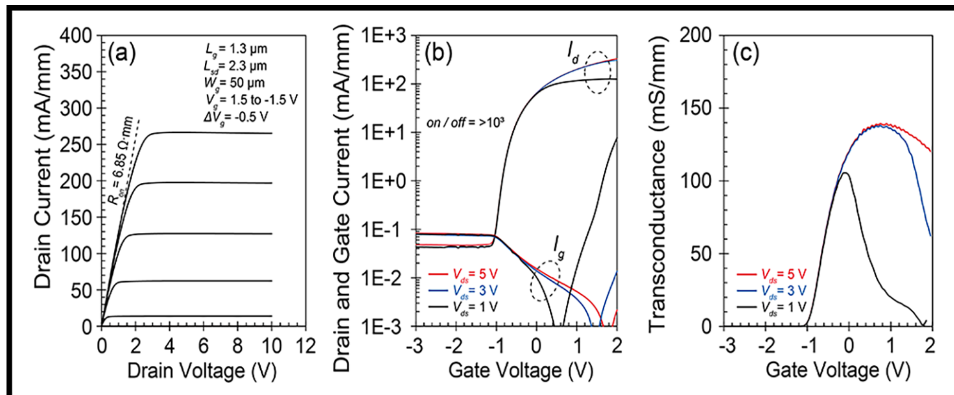

Figure 3: (a) Output I-V *curves show current saturation and an on-resistance of 6.85 Ω·mm at* V_g *= -1.5 V. (b) Log-scale transfer curves show more than three orders of* I_{on} / I_{off} *modulation, limited by Schottky gate leakage. (c) The linear-scale transfer curve shows normally-on operation and a peak* $gm_{,ext}$ *of 139 mS/mm at* V_d *= 5 V.*

Low Contact Resistance Non-Alloyed Contacts to (010) β-Ga_2O_3 for kV Radio Frequency Applications

CNF Project Number: 2802-19
Principal Investigator(s): Huili Grace Xing[1], Debdeep Jena[1]
User(s): Kathleen Smith[2]

Affiliation(s): 1. School of Electrical and Computer Engineering,
2. Department of Applied and Engineering Physics; Cornell University
Primary Source(s) of Research Funding: Air Force Office of Scientific Research (AFOSR)
Contact: grace.xing@cornell.edu, djena@cornell.edu, kts57@cornell.edu
Primary CNF Tools Used: ABM Contact Aligner, SC4500 Odd-Hour E-Beam Evaporator, Angstrom E-Beam Evaporator, RTA-AG610a, Glen 1000 Resist Strip, SAMCO UV-1 UV/Ozone, PT770, AJA Sputter Deposition

Abstract:

We demonstrate non-alloyed Ti/Au contacts to n+ (010) β-Ga_2O_3 doped by both *in-situ* doping during metal oxide chemical vapor deposition (MOCVD) and sub-oxide molecular beam epitaxy (MBE) with dopant concentrations well above 1×10^{19} cm^{-3}. The resulting contacts have sufficiently low (much less than 1 Ω-mm) contact resistance (R_c) even without alloying of the contacts.

Summary of Research:

Gallium(III) oxide (β-Ga_2O_3) has attracted interest in recent decades as a promising material candidate for kV radio frequency (RF) applications, especially in extreme environments, due to its large bandgap and critical electric field, decent carrier mobility, and availability of native substrates via melt-growth techniques. In order to enable high speed device applications, the parasitic resistance originating from the contacts should be much less than 1 Ω-mm. However, the low electron affinity associate with the wide bandgap leads to a lack of sufficiently low work-function metals to form ohmic metal-semiconductor junctions. Instead, ohmic contacts to Ga_2O_3 rely on tunnel junctions between a metal and heavily doped semiconductor region. However, the reliable formation of such junctions is non-trivial.

Previously, alloyed Ti/Au ohmic contacts were successfully formed to unintentionally doped (UID) epitaxy on semi-insulation Fe-doped (010) ion implanted with Si to a 100 nm box concentration of 5×10^{19} cm^{-3} by electron-beam evaporation and liftoff, resulting in an R_c of 0.16 Ω-mm. However, contacts formed by an identical process to MOCVD-grown Ga_2O_3 *in-situ* doped with Si to a concentration of 1.3×10^{20} cm^{-3} displayed highly rectifying behavior prior to alloying. While the contacts appeared ohmic post-alloying, the resultant contacts were spatially non-uniform, preventing extraction of R_c. We currently ascribe the abnormal behavior of these contacts to formation of a spatially non-uniform interfacial layer on the Ga_2O_3 surface.

In this work, a 102.5 nm UID buffer layer followed by 222.5 nm of Si-doped layer was grown on semi-insulating Fe-doped (010) β-Ga_2O_3 substrate via MOCVD. Room-temperature Hall measurements with In-dot contacts showed a free carrier concentration of 5.3×10^{19} cm^{-3} and a sheet resistance (R_{sh}) of 52 Ω/□. Transfer length method (TLM) patterns were fabricated using RIE for mesa isolation followed by non-alloyed Ti/Au (50/110 nm) contacts deposited by e-beam evaporation and patterned via liftoff. The as-deposited contacts were highly rectifying and spatially non-uniform.

The existing contacts were removed and Ti/Au ohmic contacts were re-deposited to form the device structure shown in Figure 1. Specific process details are anticipated for publication in the future. The resulting contacts demonstrate highly-leaky Schottky behavior, as seen in Figure 2a. At an applied current bias of 25 mA, the TLM patterns have an R_c of 0.49 Ω-mm without alloying as seen in Figure 2b.

Following this result, a 1 μm Si-doped layer was grown on semi-insulating Fe-doped (010) β-Ga_2O_3 substrate via suboxide MBE. Room-temperature Hall measurements with In-dot contacts showed a sheet resistance (R_{sh}) of 34 Ω/□. The carrier concentration was measured by secondary ion mass spectroscopy to be 2.99×10^{19} cm^{-3}. Non-alloyed Ti/Au (10/110 nm) were deposited by e-beam evaporation and patterned to form circular TLM (CTLM) patterns using a similar process to the non-alloyed MOCVD contacts. The device structure is shown in Figure 3. The resulting contacts are again highly-leaky Schottky in character, as shown in Figure 4a. At an applied current bias of 25 mA, the CTLM patterns have an R_c of 1.0 Ω-mm as show in Figure 4b, likely due to the lower doping level which naturally results in a thicker tunneling barrier and higher metal-semiconductor contact resistance.

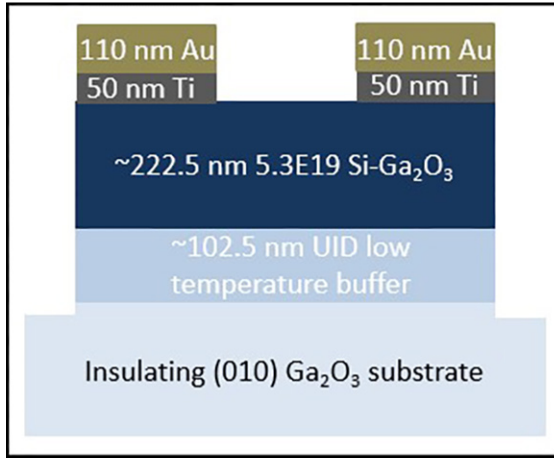

Figure 1: Device structure of the MOCVD-grown sample.

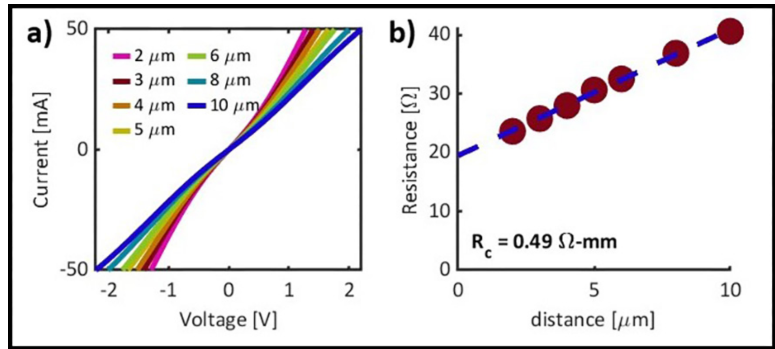

Figure 2: a) IV measurements of non-alloyed contacts display super-leaky Schottky behavior. b) TLM extraction of contact resistance at 25 mA applied current bias gives an R_c of 0.49 Ω-mm.

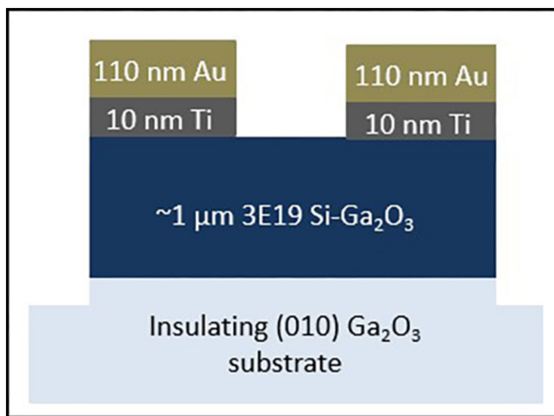

Figure 3: Device structure of the suboxide MBE-grown sample

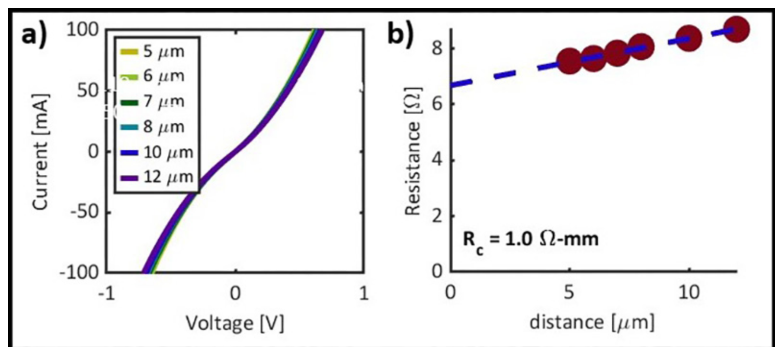

Figure 4: a) IV measurements of non-alloyed contacts display super-leaky Schottky behavior. b) TLM extraction of contact resistance at 25 mA applied current bias gives an R_c of 1.0 Ω-mm.

Conclusions and Future Steps:

In this work, we successfully demonstrate non-alloyed contacts on both MOCVD and suboxide MBE grown (010) n+ β-Ga_2O_3. Future work includes extensive characterization of the Ti/Ga_2O_3 interface to identify any interfacial layers that may have contributed to the non-uniformity observed in previous work and the initial MOCVD process. Further contact studies will extend to patterned regrowth of n+ β-Ga_2O_3 on n- doped epitaxy to investigate the resistance of the n+/n- semiconductor interface.

We acknowledge support from the AFOSR Center of Excellence Program FA9550-18-1-0529. This work was performed in part at the Cornell NanoScale Science & Technology Facility (CNF), a member of the National Nanotechnology Coordinated Infrastructure NNCI), which is supported by the National Science Foundation (Grant NNCI-2025233).

High Frequency Sensors and Actuators for Ultrasonic Imaging and Sensing

CNF Project Number: 2876-20
Principal Investigator(s): Robert Scharf, Amit Lal
User(s): Anuj Baskota, Justin Kuo, Scott Zimmerman

Affiliation(s): Geegah Inc.

Primary Source(s) of Research Funding: DARPA, ARPA-E, DOE

Contact: rms248@cornell.edu, amit@geegah.com, anuj@geegah.com, justin@geegah.com, scottez@geegah.com

Website(s): www.geegah.com

Primary CNF Tools Used: Olympus BX-51 Fluorescence Microscope, Zygo Optical Profilometer, VersaLaser Engraver, Harrick Plasma Generator

Abstract:

Geegah, Inc., specializes in developing ultrasonic imagers that are compatible with complementary metal-oxide-semiconductor (CMOS) technology and operate at gigahertz (GHz) frequencies. These imagers are designed with an array of transducers made with thin film of aluminum nitride (AlN), each measuring 50 × 50 μm. The acquisition of high-resolution images consisting of 128 × 128 pixels can be performed at a sampling rate up to 20 fps. Geegah's technology finds applications in diverse fields. It can be used in agriculture for soil imaging [1] and nematode detection [2]. It also enables the monitoring of fluid flow and mixing [3] of colorless liquids in opaque substrate microfluidic channels. Other applications currently being explored include lens imaging [4], microbes and biofilm analysis, water quality sensing, tissue imaging [5], and skin analysis. While the imaging chips are manufactured in a commercial CMOS foundry, early packaging of these systems was done in CNF. Furthermore, other packaging and analysis tasks performed in CNF include fabrication and bonding of Polydimethylsiloxane (PDMS) microfluidic channels on Geegah chips, fluorescence imaging to validate biofilm growths, and height profile analysis of thin films on imaging surface.

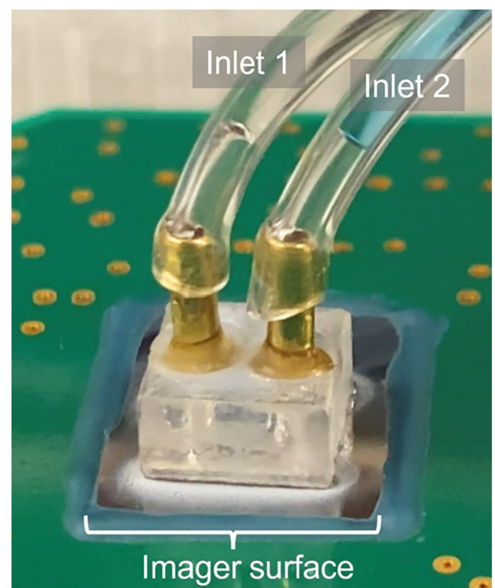

Figure 1: Ultrasonic imager with a microfluidic chip attached to the sensing surface.

Summary of Research:

Microfluidic channels on-chip enable real-time visualization of fluid flow and mixing based on the acoustic impedance differences between the liquids. This enables monitoring photo-sensitive liquids in dark, transparent fluids without the aid of color dyes, and visualization of fluids inside opaque microfluidic channels. The device that consists of a semi-transparent microfluidic channel bonded on the imager chip is shown in Figure 1. Various shapes of channels were patterned on PDMS molds using the VersaLaser Engraver and plasma bonded to the silicon surface using Harrick Plasma Generator. This device is then used to visualize mixing of two transparent liquids, alcohol and water, as shown in Figure 2. Note the benefit of acoustical approach when it comes to imaging of optically transparent liquids as the captured contrast stems from the acoustical impedance differences, not from the differences in optical properties.

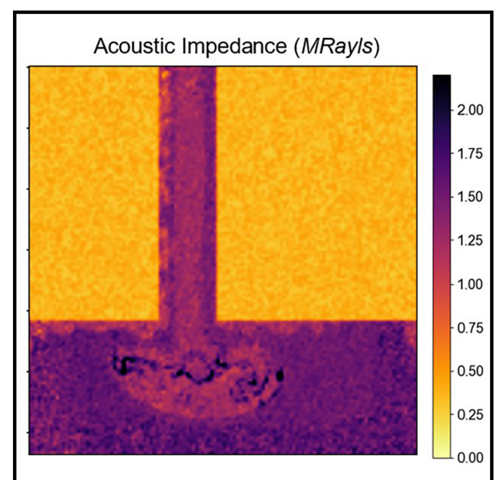

Figure 2: Acoustic impedance map showing jet of ethanol (99%) mixing with water in microfluidic channel captured at 1.853 GHz.

Conclusions and Future Steps:

Overall, various applications have been demonstrated using the GHz ultrasound imaging technology, including but not limited to microfluidics monitoring, biofilm tracking, soil sensing, and tissue imaging. The visualization of structures/layers, in addition to the measurement of acoustic impedance, enables the exploration of various biological and chemical processes using this novel chip. In the future, various patterned PDMS structures as well as other substrates will be attached and tested on the Geegah imager. Furthermore, chemical reactions forming precipitates along with exothermic and endothermic reactions will be monitored using GHz ultrasound imaging.

References:

[1] Baskota, A., Kuo, J., Ardanuç, S., and Lal, A. 2022, October. Nematode Species Differentiation Using GHz Ultrasonic Micro-Imager. In 2022 IEEE International Ultrasonics Symposium (IUS) (pp. 1-4). IEEE.

[2] Baskota, A., Kuo, J., and Lal, A., 2022, January. Gigahertz Ultrasonic Multi-Imaging of Soil Temperature, Morphology, Moisture, and Nematodes. In 2022 IEEE 35th International Conference on Micro Electro Mechanical Systems Conference (MEMS) (pp. 519-522).

[3] Baskota, A., Kuo, J., Ardanuç, S., and Lal, A. (2023, June). Visualization Of Fluid Mixing Using GHz Ultrasonic Imaging. In 2023 22nd International Conference on Solid-State Sensors, Actuators and Microsystems (Transducers).

[4] Hwang, J., Baskota, A., Davaji, B., Kuo, J., and Lal, A. (2022, October). Gigahertz Metamaterial Ultrasonic Lens Characterization Using GHz CMOS Integrated Ultrasonic Micro Imager. In 2022 IEEE International Ultrasonics Symposium (IUS) (pp. 1-4).

[5] Baskota, A., Kuo, J., Ardanuç, S., and Lal, A. (2023). Compact GHz Ultrasonic Micro-Imager for Cells and Tissues. Microscopy and Microanalysis, 29(Supplement_1), 1116-1117. https://doi.org/10.1093/micmic/ozad067.572.

Developing a Passivation-First Recessed T-Gate Procedure for AlN/GaN/AlN HEMTs

CNF Project Number: 2975-21
Principal Investigator(s): Austin Hickman
User(s): Austin Hickman, Shankar Miller-Murthy

Affiliation(s): Soctera Inc.
Primary Source(s) of Research Funding: National Science Foundation (NSF)
Contact: austin.hickman@soctera.edu, shankar.murthy@soctera.com

Primary CNF Tools Used: I-line stepper, PT770 Etcher, Oxford 81 Etcher, Odd hour E-beam evaporator, JEOL 6300 EBL, Oxford PECVD, AJA Sputter Deposition, Woolam Ellipsometer, Zeizz Ultra SEM, Leica Critical Point Dryer, Glen1000 resist stripper, P7 profilometer

ELECTRONICS

Abstract:

In this work, we report functional recessed T-gate structures fabricated using a procedure compatible with the AlN/GaN/AlN structure. The devices were fabricated on an AlGaN/GaN chip using a combination of gentle fluorine-based plasma etching and a buffered oxide etch (BOE) wet process to selectively remove passivation without implanting fluorine-based trap states. The devices demonstrated on-currents over 1.15 A/mm with an on-resistance of 1.8 Ω·mm. Transfer characteristics revealed I_{on}/I_{off} ratio of 10^4 and peak transconductance of 0.3 S/mm.

Summary of Research:

Next-generation (6G) wireless communication and high-resolution radar systems target high-power operation in the terahertz regime. Gallium nitride high-electron-mobility transistors (GaN HEMTs) are well-suited for this high-power, high-frequency application. However, the conventional AlGaN/GaN heterostructure provides poor quantum confinement of the two-dimensional electron gas (2DEG), generating short channel effects at high frequencies. Additionally, its RF power performance is limited by the breakdown voltage. The AlN/GaN/AlN heterostructure offers material and device design advantages over the conventional AlGaN/GaN HEMT: the AlN buffer tightly confines the 2DEG and offers a higher thermal conductivity path than a thick GaN buffer, and the AlN barrier induces higher density 2DEGs at thinner distances (5 nm). AlN also maximizes the barrier bandgap, improving breakdown voltage.

Recently, fully realized T-gated AlN/GaN/AlN HEMTs were fabricated and characterized. The T-gates were defined via two-stage electron beam lithography using a single followed by a double-layer resist stack. The first single-layer resist was used to define the gate stem combined with a chrome mask layer to ensure vertical side-walls, which was etched out of the SiN passivation using a combination of SF_4 plasma etching and a single minute of buffered oxide etch exposure to remove the last remaining SiN and expose the AlGaN without implanting any ions. The resulting structure is shown in Figure 1. The second, double-resist electron beam lithography exposure was used to define the head area, where Ni/Au (50/200 nm) gate metal was deposited via e-beam evaporation. The resulting structure is shown in Figure 2.

The devices demonstrated on-currents over 1.15 A/mm with an on-resistance of 1.8 Ω·mm. Transfer characteristics revealed I_{on}/I_{off} ratio of 10^4 and peak transconductance of 0.3 S/mm. All DC characteristics are shown in Figures 3 and 4.

These positive results, even at this early stage of the project, illustrate the effectiveness of this technique. With some refinement, it may allow the AlN platform to enable the next generation of high-power, mm-wave communication.

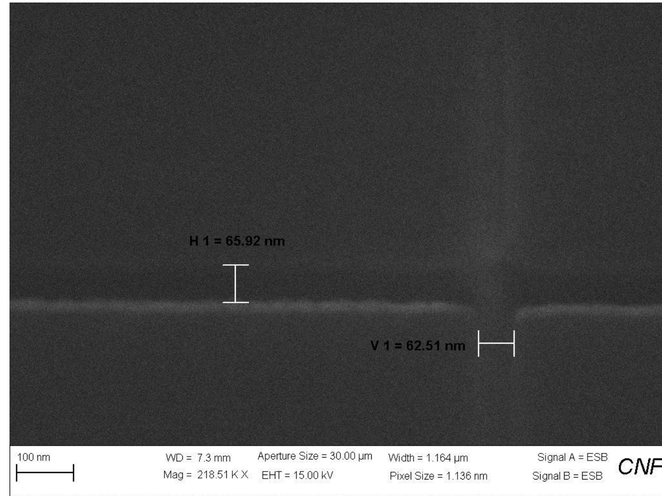

Figure 1: T-gate stem trench demonstrating a gate length of 65 nm.

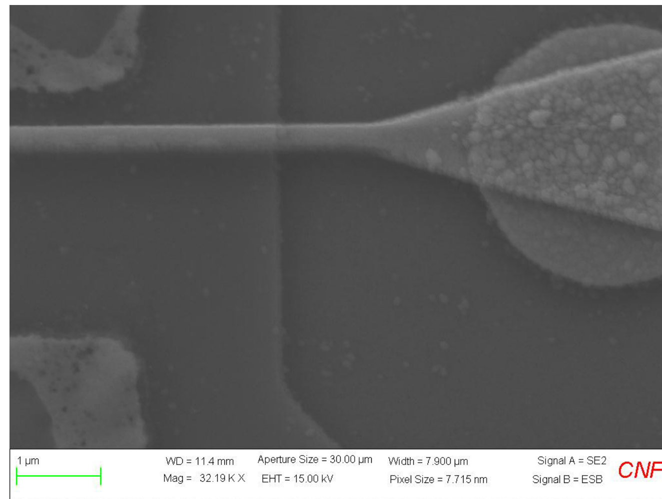

Figure 2: T-gate head with buried trench demonstrating a gate head width of ~250 nm.

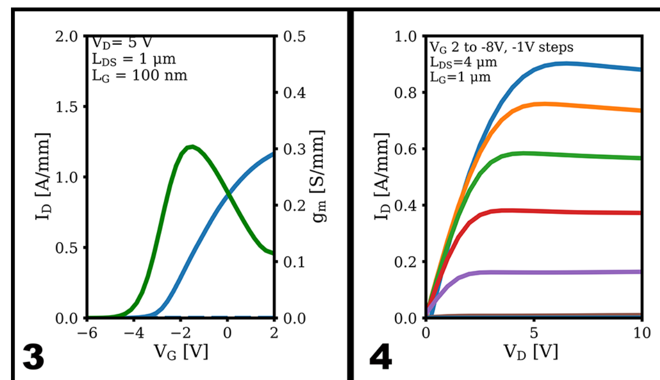

Figures 3 and 4: DC characteristics for AlGaN/GaN recessed T-Gate HEMT.

Redistribution Layers on Glass Wafers

CNF Project Number: 3018-22
Principal Investigator(s): Dr. Shelby F. Nelson, Dr. Lee Tutt
User(s): Dr. Lee Tutt

Affiliation(s): Mosaic Microsytems, LLC

Primary Source(s) of Research Funding: Commercial revenue from early prototypes

Contact: shelby.nelson@mosaicmicro.com, lee.tutt@mosaicmicro.com

Primary CNF Tools Used: Photolithography suite (both spinning and laminating photosensitive materials, and align & develop), CHA Mark50 for evaporation of metals, thermocompression bonder

Abstract:

Mosaic Microsystems is a small company with cleanroom facilities in Rochester NY, specializing in thin glass interposers for the microelectronic packaging industry. Mosaic has used CNF primarily for early exploration of interconnect metallizations. As a small company bringing up many processes simultaneously in-house, Mosaic was grateful for the already-functional facilities offered by the CNF to be able to explore tools and processes for early prototypes. For a variety of customer projects, some one-off and others early versions of processes that may become main-stream for Mosaic, the access to good equipment that is well maintained accelerated our delivery and helped build our business.

Summary of Research:

Mosaic has a proprietary process for bonding thin glass to a handle wafer, allowing the thin glass to be processed in mainstream semiconductor equipment. Mosaic used CNF to metallize and pattern such bonded glass wafers with platinum, copper, aluminum, tantalum, titanium, and gold. In some cases, Mosaic used the thermocompression bonder to create multilayer glass stacks. Even such relatively "standard" processes must be adapted for new materials, and Mosaic has been very grateful to have the Cornell NanoScale Facility relatively near-by to allow explorations when we have not yet been able to bring similar equipment up in our own cleanrooms.

Conclusions:

In the world of semiconductor packaging, small companies face a significant challenge in acquiring sufficient capital equipment to build the business at a rate that allows the business to grow. Having access to the CNF equipment and expertise has been highly valuable.

D-Band Filters and Splitters Based on SiC Substrate-Integrated Waveguides

CNF Project Number: 3078-23
Principal Investigator(s): James C.M. Hwang
User(s): Xiaopeng Wang

Affiliation(s): School of Electrical and Computer Engineering, Department of Materials Science and Engineering; Cornell University

Primary Source(s) of Research Funding:

Contact: jch263@cornell.edu, xw569@cornell.edu

Primary CNF Tools Used: ABM Contact Aligner, SÜSS MA6-MB6 Contact Aligner, AJA Sputter Deposition - 1 & 3, AJA Ion Mill, Electroplating - Au & Ni

Abstract:

The objective of this project is to demonstrate the feasibility for monolithic integration of antennas, filters, and high-electron mobility transistors (HEMTs) on SiC. To demonstrate that individual components survive the monolithic integration, the D-band filters based on SiC substrate-integrated waveguides (SIW) are designed, fabricated, and measured. The resulted D-band (110.170 GHz) SIWs exhibit a record low insertion loss of 0.22 ± 0.04 dB/mm, which is four times better than that of the GCPWs. A 3-pole filter exhibits a 1.0-dB insertion loss and a 25-dB return loss at 135 GHz, which represents the state of the art of SiC SIW filters and is order-of-magnitude better than Si on-chip filters. The compact filters are designed, fabricated, and measured but exhibit high insertion loss due to the high resistance of the through-substrate vias (TSVs). Solid TSVs can minimize the resistance of the TSVs and thus decrease the insertion loss. The new process is under development and optimization. The D-band splitters are designed and will be fabricated and measured.

Summary of Research:

SiC SIWs are attractive because high-power and high-efficiency GaN amplifiers are usually fabricated on SiC. SiC is high in dielectric constant, electrical resistivity, breakdown strength, mechanical toughness, and thermal conductivity, but low in loss tangent and thermal expansion coefficient. Previously, for proof of principle, we used the custom process at Cornell University to design and fabricate a 3-pole filter comprising three SIW resonators, which exhibited a 1-dB insertion loss and a 25-dB return loss at 135 GHz [1]. These record performances (Table I and Table II) make SIW promising for monolithic integration of high-quality SIW filters, edge-firing SIW antennas, and GaN HEMTs as shown in Figure 1.

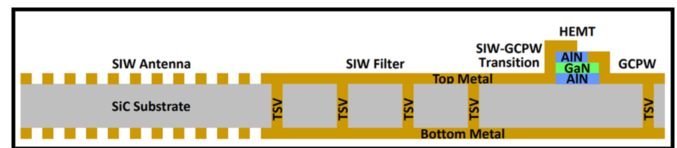

Figure 1: Schematics of an MMIC with an edge-firing SIW antenna, an SIW filter, and a GaN HEMT on the same SiC chip.

The first custom process is using Ni/Al as the top and bottom metal because of the limitation of the CNF tools. On the other hand, sidewalls of the TSVs are covered by sputtering Al. To further reduce the conductor loss, Au was used to replace the Al as the bottom metal. The Au is deposited planetary evaporation to cover the sidewalls of the TSVs. Since the depth of the TSV is 100 μm while the TSV diameter is 50 μm, the Au cannot cover the TSVs due to such high aspect ratio as depicted in Figure 2. The solid TSVs by electroplating Au could solve this issue but needs better control of the ICP-RIE etching of the SiC substrate. The etching recipe has been successfully transferred to Notre Dame.

In addition to the changes in metal, 4" SiC wafers are replacing the small chips (1 cm by 1 cm). The hard mask is critical for the ICP-RIE etching. Ni is the typical choice with the high selectivity and simple process. The SiC substrate is 100 μm in thickness which requires at least 3.3-μm thick Ni hard mask. In the first custom process, pure Ni was sputtered on small chips as the seed layer for Ni electroplating. When handling the 4" SiC wafers, the pure Ni seed layer cannot sustain such high stress strength from the 3.3-μm Ni. The combination of Ti and Ni can bear high stress strength from the thick Ni. The potential problem along with Ti is that Ti is hard to get removed thoroughly and if it's the case, the following ICP-RIE etching will fail and the whole wafer will be useless.

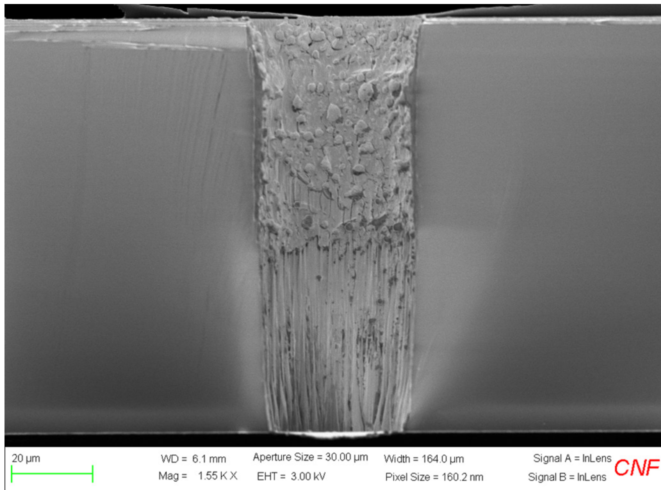

Figure 2: SEM image of the cross-section of the TSV after Au planetary evaporation.

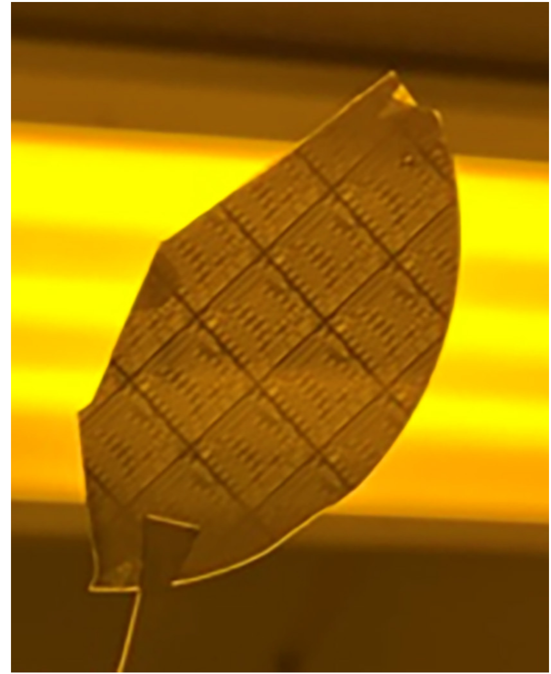

Figure 3: SiC test chip after ICP-RIE etching.

The test has been performed with the sequential processes of Ti/Ni seed layer sputtering, Ni hard mask electroplating, Ion mill, and then ICP-RIE etching. The results have proved that Ti will not affect the SiC etching as shown in Figure 3.

Conclusion and Future Steps:

The compact filters are designed, fabricated, and measured exhibiting high insertion loss due to the high resistance of TSVs. The new process on 4" SiC wafers are under development using Au for top and bottom metal layer, solid TSVs by electroplating Au. Meanwhile, the D-band splitters are designed. The new masks including filters and splitters are prepared. Each individual process has been validated except the Au electroplating on the 4" SiC wafers.

The new run of fabrication has started and will move on if the tools in CNF work well. The Au electroplating will be verified. The measurement will be performed in HFTL (Bard 315) using the 220 GHz single-sweep probe station system at Cornell University and banded probe station system in University of Notre Dame, respectively, for cross check and validation.

References:

[1] M. J. Asadi, L. Li, K. Nomoto, Y. Tang, W. Zhao, P. Fay, D. Jena, H. G. Xing, and J. C. M. Hwang, “SiC Substrate-Integrated Waveguides for High-Power Monolithic Integrated Circuits Above 110 GHz,” 2021 IEEE MTT-S Int. Microw. Symp. (IMS), Atlanta, GA, USA, 2021, pp. 669-672.